Title: **Molecular mechanism of Arp2/3 activation by nucleation promoting factors and actin monomer**

Sahithya Sridharan Iyer[a], Jiangbo Wu[a], Thomas D. Pollard[b,c,d,*,1], and Gregory A. Voth[a,1]

[a]Department of Chemistry, Chicago Center for Theoretical Chemistry, Institute for Biophysical Dynamics, and James Franck Institute, The University of Chicago, Chicago, IL
[b]Department of Molecular Cellular and Developmental Biology, Yale University, CT
[c]Department of Molecular Biophysics and Biochemistry, Yale University, New Haven, CT
[d]Department of Cell Biology, Yale University, New Haven, CT
*Current address: Department of Cell and Molecular Biology, University of California, Berkeley

[1]Corresponding Authors: E-mail: gavoth@uchicago.edu; thomas.pollard@yale.edu

Supporting Information

Structures with PDB IDs	**Arp2-Arp3 distance (Å)**	**Arp3 dihedral angle (°)**	**Arp2 dihedral angle (°)**	**Clamp dihedral angle (°)**
6UHC; human Arp2/3 complex bound to two copies of *Mus musculus* N-WASP-CA	53.8	-18.8	-8.6	-50.4
6UHC after 37 ns pre-equilibration at 310K	54.7	-24.3	-6.1	-45.2
6UHC after 3.4 µs of simulation at 310K	52.7 (51.2,56.1)	-34.0	-19.6	-33.1 (-52.0 to -22.7)
4JD2; inactive *Bos taurus* Arp2/3 complex	52.4	-20.8	-18.2	-50.6
4JD2 after 37 ns pre-equilibration at 310K	54.1	-28.5	-18.7	-42.7
4JD2 after 2.2 µs of simulation at 310K	54.3 (52.8 to 55.5)	-25.2	-23	-36.5 (-50.7 to -24.7)
7T5Q; *Bos taurus* Arp2/3 complex bound to an actin monomer and CapZ with the N-WASP CA motif fused to the α and β subunits	50.4	-18.1	-13.1	-39.9
7T5Q after 37 ns pre-equilibration at 310K with actin and without CapZ	49.4	-23.9	-10.1	-38.8
7T5Q after 1 µs of simulation at 310K with actin and without CapZ	48.8 (45.6 to 50.9)	-18.2	-20.5	-26.5 (-38.2 to -11.7)
7T5Q after 930 ns of simulation at 310Kwithout actin or CapZ (rep1)	53.8 (48.8 to 55.9)	-17.6	-11.6	-41.8 (-49.2 to -16.4)

Table S1: Conformational parameters of three cryo-EM structures used to start MD simulations, after 37 ns of pre-equilibration and after MD simulation production runs. Minimum and maximum distances and clamp dihedral angles sampled during the production run are given in brackets. The Arp2-Arp3 distance is the distance between the centers of mass of subdomains SD3 and SD4 of Arp2 and Arp3. For reference, this distance along the short-pitch helix of an actin filament is 42.1 Å. The dihedral angles of Arp2 and Arp3 are defined by the centers of mass of subdomains SD2-SD1-SD3-SD4. The clamp dihedral angle measures the rotation of the two blocks of structure in Arp2/3 complex relative to each other. It is defined by four points (centers of mass of residues K18 and I244 of ArpC2 and R32 and S147 of ArpC4. The clamp dihedral angle in the branch junction structure is -19.0°. During the 200 ns MD simulation of Arp2/3 complex extracted from the branch junction, the clamp dihedral angle fluctuated between -13.2° to -32.0° while the Arp2-Arp3 distance fluctuated between 39.8 Å to 41.9 Å.

Section 1: Comparison of CA bound and free Arp2/3 complex

We compared a control 3.2 µs MD simulation of inactive bovine Arp2/3 complex without CA (pdb id: 4JD2) with our 3.3 µs MD simulation of CA bound human Arp2/3 complex (pdb id: 6UHC). While Arp2/3 complex with CA bound shifts toward the partially active state (also shown in Fig. 5A), Arp2/3 complex without CA (control) did not (Fig. S1).

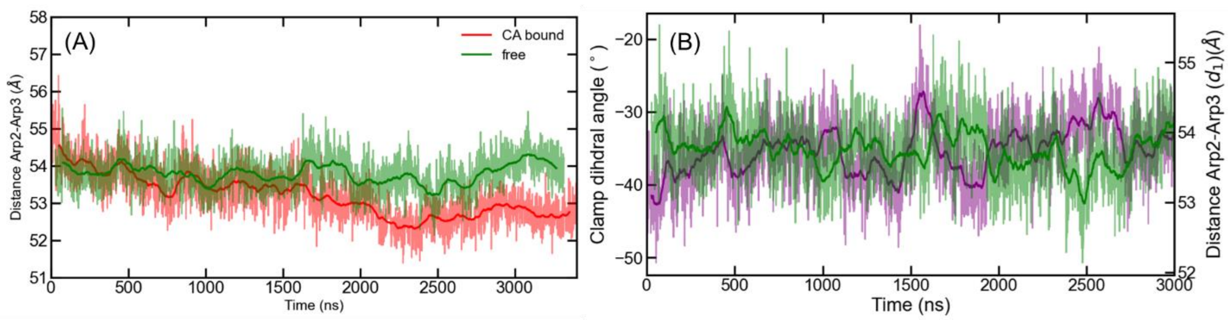

Figure S1: Conformations of inactive Arp2/3 complex without bound CA during 3.2 µs of MD simulation. (A) Comparison of changes in distances between the centers of mass of subdomains 3 and 4 of Arp2 and Arp3 without (green) and with bound CA (red). Without bound CA the distance fluctuates about an average of 54.3 Å. With CA bound the distance decreases during the simulation. (B) The clamp dihedral angle for the control system (purple) fluctuates around -36.5°. Lighter traces are values during the simulations and solid lines are their running averages with a window of 50 ns.

Section 2: Free energy sampling of conformational changes along the pathway of branch formation by Arp2/3 complex

This section provides additional information about the free energy calculations of the pathway of branch formation (Fig. 2). Free energies of Arp2/3 complex during branch formation are calculated using a combination of metadynamics (path CV S=1-11), umbrella sampling (path CV S=6.5-11) and equilibrium unbiased MD simulations (path CV S=11-12) (Fig S2A,B). Free energies in Fig. S2B are appended to the average of free energies in Fig S2A to obtain the free energy of the branch junction formation. Convergence of the metadynamics simulations was determined by multiple crossings between the two end states (Fig. S2C, G-J), the decrease in hill height (Fig. S2E) and stable PMF in the last 20ns of the simulation (Fig. SF). Additionally, short equilibrium MD runs starting from different conformations on the free energy surface were run to determine its stability (Fig. S2 K-M).

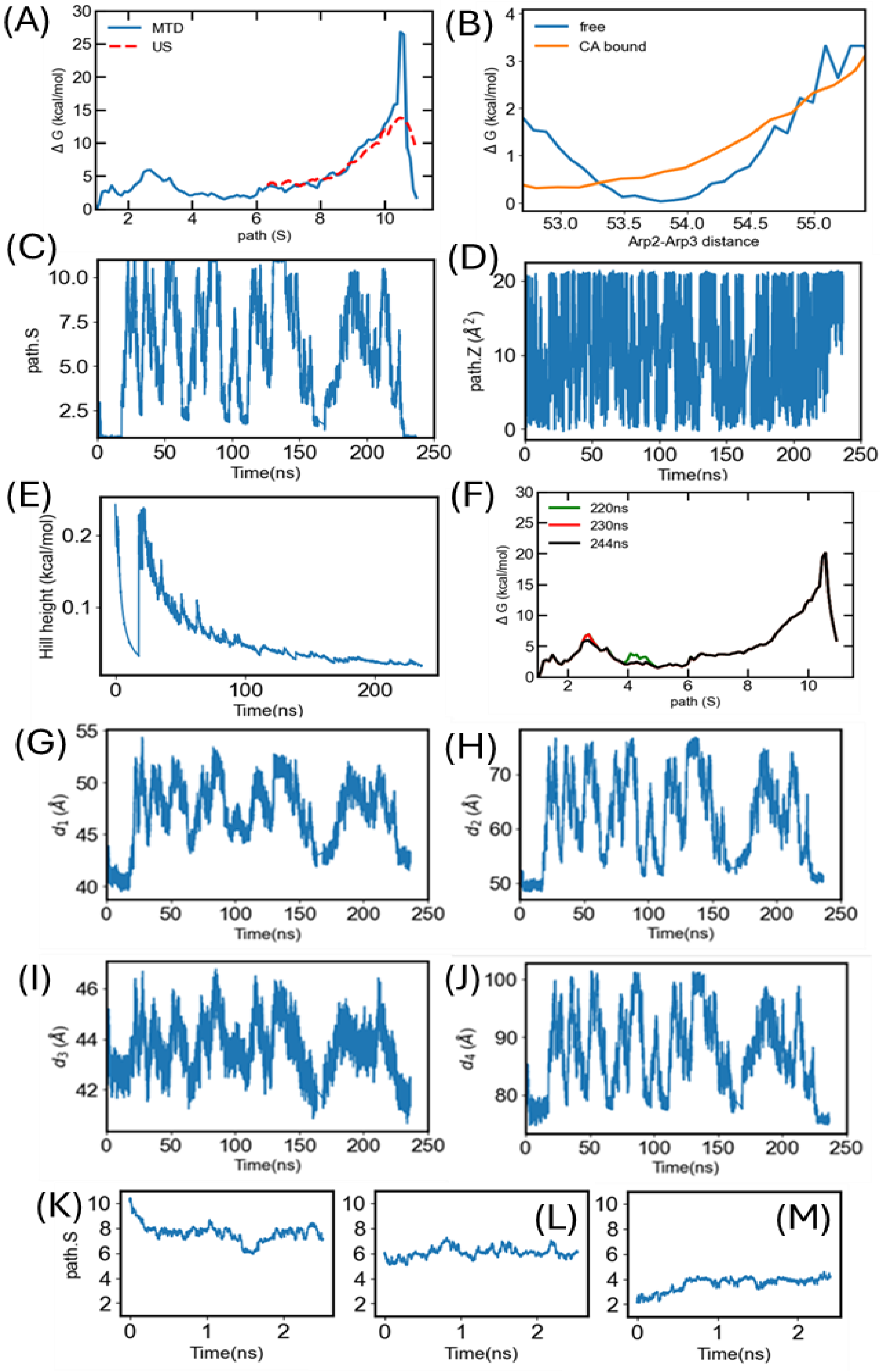

Figure S2**:** (A) Reweighted free energies calculated from metadynamics (blue) and umbrella sampling (red) simulations of Arp2/3 complex along the path collective variable (S) from the branch junction at state 1 to partially active state 11. Umbrella sampling in the region between states 6.5 and 11 was done with conformations taken from the metadynamics simulation. (B) Free energy calculated from the probability distribution obtained from 2.2 µs MD simulation of free inactive Arp2/3 complex (pdb id: 4JD2) and CA bound inactive Arp2/3 complex (pdb id:6UHC). The equilibrium simulations correspond to path S between 11 and 12. CA binding lowers the free energy of the partially active state and enables the transition to partially active state. (C) During 240 ns of well-tempered metadynamics simulation, Arp2/3 complex fluctuated multiple times between the active state (1) and partially active (11). path S shown on the x-axis is the collective variable used for sampling. This indicates free diffusion of the CV between the two extreme states. (D) Variation in path.Z values sampled during the metadynamics simulation with an upper wall placed at path.Z value of 20 Å^2. (E) Decrease in the hill heights during 240 ns of well-tempered metadynamics simulation. (F) PMF calculated three times during the last 24 ns of the metadynamics simulation (G-J) Sampling of four distances d_1 to d_4 during the metadynamics simulation. The set values for the distances had these ranges: d_1 40.8 Å to 53.2 Å, d_2 50.1 Å to 73.2 Å, d_3 42.2 Å to 46.4 Å and d_4 79.2 to 99.8 Å. (K-M) PathCV sampled in equilibrium MD simulations starting from different conformations on the free energy landscape. (K) Starting from the high free energy conformation (path.S = 10.2), the transition to lower free energy conformation of path.S value of 7 occurs within 1 ns of equilibrium MD. (L) Starting from a conformation corresponding to path.S value of 6.1, the conformation fluctuates between 6-7 during the 2 ns of equilibrium MD simulation. (M) Starting from a conformation corresponding to path.S value of 2.4, the conformation transitions to a lower free energy conformation of path.S value of 4 in the 2 ns of equilibrium MD simulation.

Conformations sampled in the high free energy region in the Umbrella Sampling simulations:

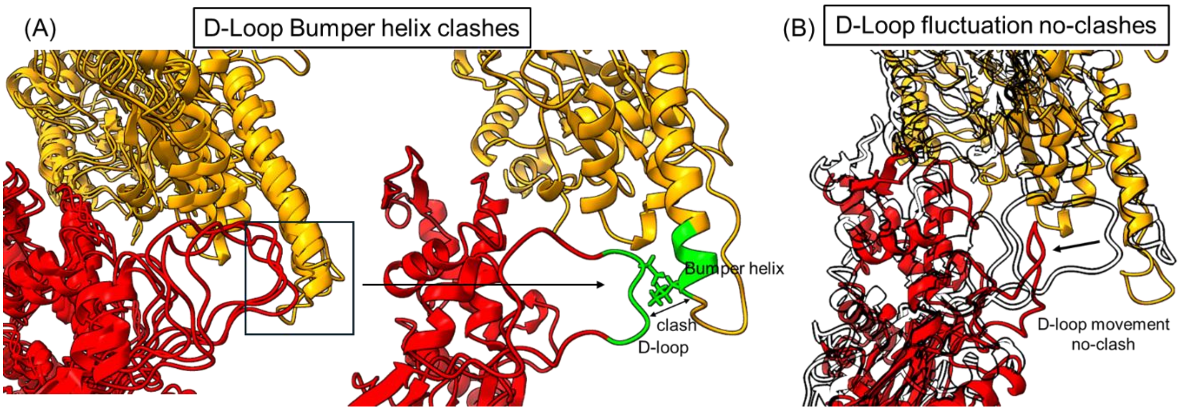

Figure S3. Ribbon diagrams with examples of conformations of the Arp2 D-loop and Arp3 bumper helix in the Umbrella Sampling (US) simulation window at the energy barrier during the transition to the short-pitch conformation. (A) The left panel shows representative conformations with clashes between the D-loop and bumper helix. The right panel shows one of these conformations with the clashing residues in green. (B) Comparison of ribbon diagrams with a D-loop conformation that does not clash with the bumper helix (red) with another where the D-loop clashes with the bumper helix (black outline). The arrow shows how fluctuations in the D-loop conformation move the D-loop away from bumper helix.

Section 3: Contacts between inactive Arp2/3 complex with the C helix and EWE motif at the C-terminus of CA persist in all atom MD simulations

Residues I463, L467, V470 and M471 on the hydrophobic face of the C helix contact different residues on Arp2 and Arp3 in the cryo-EM models of human Arp2/3 complex bound to two copies of *Mus musculus* N-WASP-CA (pdb id: 6UHC). The contacts of Arp2 are residues Y147 on the hinge helix, G150 and L151 on the loop following the hinge helix and L361, I364 and M365 on the helix adjacent to the hinge helix. The contacts on Arp3 are residues A150, A151, W153 on the hinge helix and residues F379, M383, L384, T387 on the helix adjacent to hinge helix and F414 at the C-terminus.

Three long-equilibrium MD simulations of this structure covered 3.4, 1.0 and 1.0 microseconds. The contacts between the C-helices and the Arps in the starting structure were preserved in the 3.4 μs simulation (Fig. S2A,B), justifying the approximate fitting of the C motif (1, 2). The stability of the contacts between C-helix and residues on Arps is quantified by the persistence time of their interactions. Contacts with residues Y147, G150, L151, L361, I364 and M365 on Arp2 and A150, A151, W153, F379, M383, L384, T387 and F414 persist for more than 1 μs in the 3.4 μs simulation (Fig. S2A,B). During the long simulation of the cryo-EM model new contacts formed between C-helix M471 and Arp3 residues H370, M372 and between V470 with Arp3 F379 on the helix adjacent to hinge helix (Fig. S2C). Mutation of the interacting residues in C helix to alanine impairs the ability of VCA to bind and activate branch formation by Arp2/3 complex (1).

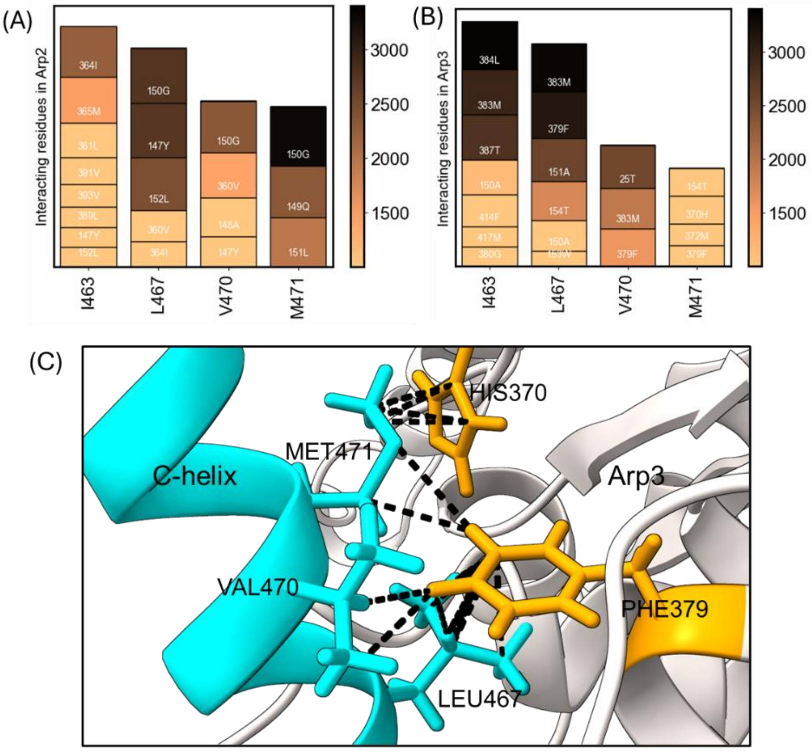

Figure S4. Contacts between the closest atoms within a cut-off of 4 Å between residues I463, L467, V470 and M471 on C-helix with residues on the Arps that persisted for more than 1 µs during the 3.4 µs MD simulation. Colorbars and heights of the boxes represent total times that the CA residues contacted Arp residues identified by white numbers in the boxes. Height of the bar represents promiscuity of the interactions. (A) Interactions with Arp2 residues. (B) Interactions with Arp3 residues. (C) Ribbon diagram showing contacts that formed between the C-helix (cyan) and Arp3 (light grey secondary structure) during 3.4 µs of MD simulation. New contacts that do not appear in the cryo-EM model (pdb id:6UHC) include M471 with H370, M471 and V470 with F379 on the helix adjacent to hinge helix (orange).

The strong interactions of ^{498}EWE^{500} at the C-termini of A with Arp3 and ArpC1 are preserved during the 3.4 µs MD simulation. As in the cryo-EM reconstruction (2) and a crystal structure of Arp3 (3) W499 is sandwiched in a "stacked-like" complex between P236, R333, and R334 of Arp3 (Fig. S3A,B,F) and proline P180, S187, K188, and M189 of ArpC1 (Fig. S3C,D,E). These interactions are important as mutation of the tryptophan to serine eliminates binding of VCA to Arp2/3 complex (4).

In Arp3, CA W499 sits in a pocket lined by V234, C235, P236, D330, R333, R334, and R337 (Fig. S3B,F). Contacts of these amino acids within 4.0 Å of W499 persist during the simulation. E498 and E500 form salt bridges with K240 and R337 (Fig. SF). In ArpC1, CA W499 sits in a pocket lined by V155, S170, Y172, P180, T183, G186, S187 K188, M189 and M195 in the loops joining the anti-parallel beta sheets of blade 4 (Fig. S3D,E). These amino acids form persistent contacts within 4.0 Å of W499 (Fig. S3E). CA E498 and E500 form salt bridges with R179 and K188 in ArpC1.

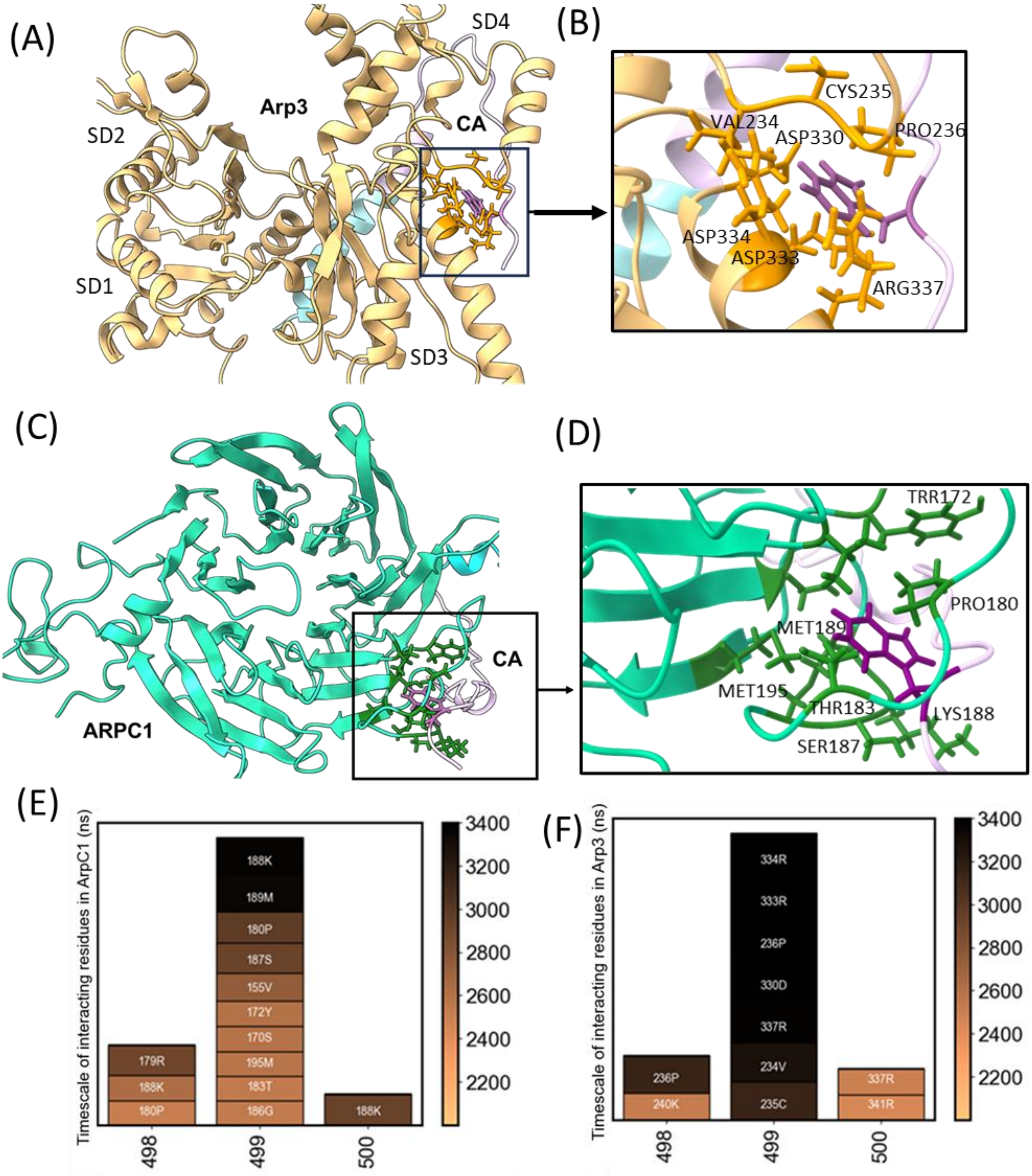

Figure S5: Interactions of the EWE motif of CA (C-helix cyan, A purple) with ArpC1 and Arp3. (A,B) Interactions with Arp2. W499 sits in a pocket lined by V234, C235, P236, D330, R333, R334, and R337. The side chain of W499 is sandwiched between P236 and R334 and R333 of Arp3. (C,D) Interactions with ARPC1. W499 sits in a pocket lined by V155, S170, Y172, P180, T183, G186, S187, K188, M189 and M195 in the loops joining the anti-parallel beta sheets of blade 4. The W499 sidechain is sandwiched between P180 and S187, K188, M189 of ArpC1. (E,F) Color bars represent durations of the contacts of EWE with (E) ArpC1 and (F)Arp3. The listed contacts were within a cut-off of 4.0 Å and persisted for more than 2 µs. Heights of the bars represents the promiscuity of the interactions.

Section 4: Interaction of A motif D/E loops with Arps and ARPC1

The D/E loops of the A motif are more flexible than the C motifs (Fig. S4 A,B) as indicated by their large RMSD values .

D/E loop interactions with Arp2/ArpC1: residues D482 to E490 of the D/E loop interact with K299, K336, K339, R343 and K341 in subdomain 3 of Arp2 and residues E491 to D497 interact with R118, K139, R142, K174, R179 and K188 in the loop connecting the anti-parallel beta strands in beta propeller blade 3 and 4 of ArpC1(5, 6) (Fig. S4C,D). Mutations K299E of Arp2 and K139E of ArpC1 impair activation of Arp2/3 complex (2). Conserved phenylalanine F493interacts with ARPC1 through stacking with P190 and a transient hydrogen bond of its backbone amide with the carboxylate oxygen of ARPC1 E193. Backbone carbon atoms of E494 and D495 interact hydrophobically with ARPC1 P190 (Fig. S4F).

D/E loop interactions with Arp3: D/E loop residues D490 to D497 interact with positively charged residues K244, K251, K254, R329, R333 and H371 in subdomain 3 of Arp3. Interactions of D/E loop residues D480 to D489 with Arp3 as less stable (Fig. S4E). Conserved D/E loop phenylalanine F493 makes stacking interactions with Arp3 residue W252 (Fig. S4G).

The salt-bridges of the D/E loop are more numerous and persistent with Arp2/ArpC1 than Arp3. Hence the electrostatic interactions of A motif of N-WASP with Arp2/ArpC1 are more favourable than with Arp3 (Fig. 3D), contributing to the higher affinity for Arp2/ArpC1 than Arp3.

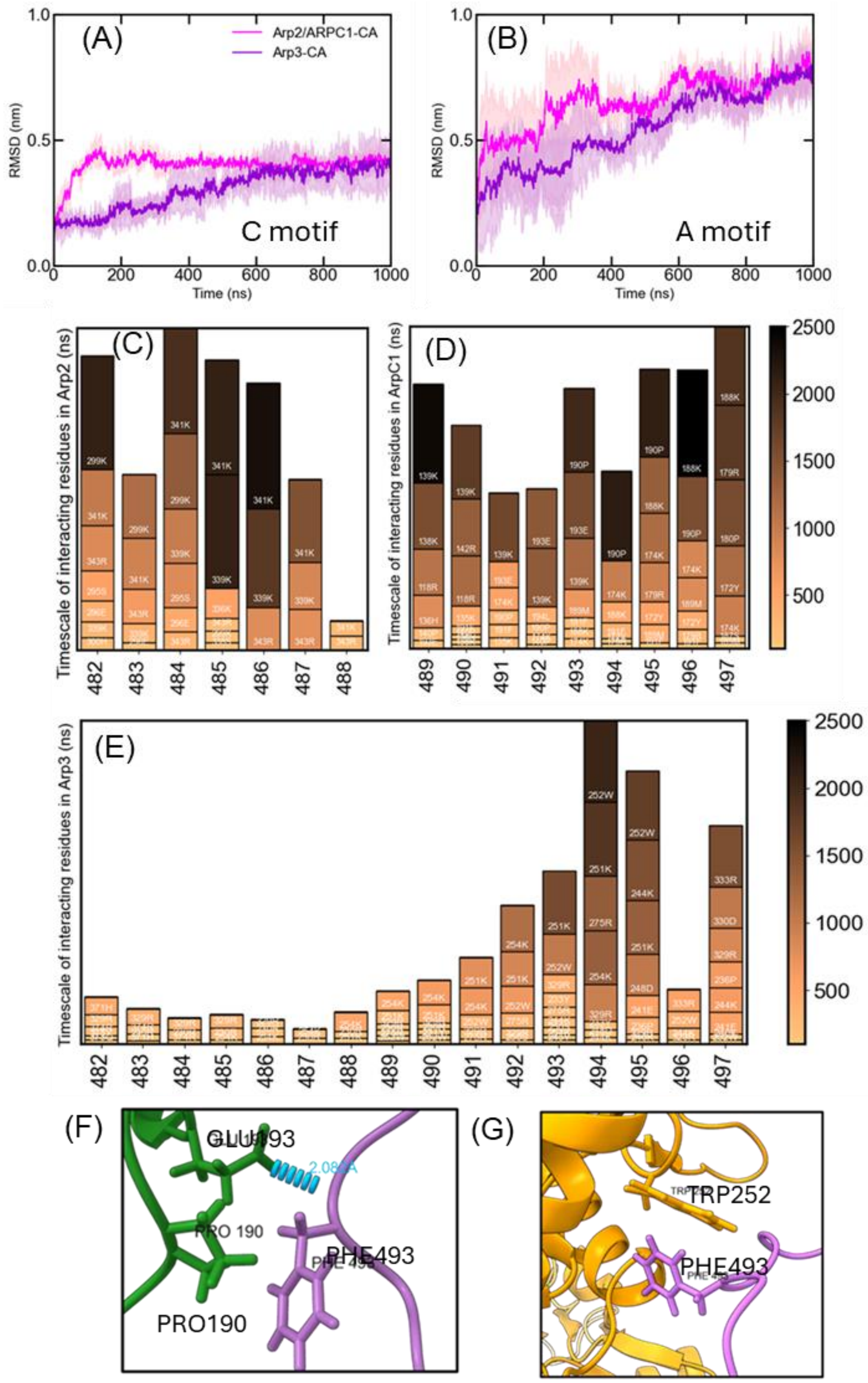

Figure S6: D/E loop conformations during MD simulation of inactive Arp2/3 complex with two bound CA motifs. (A, B) Time courses RMSD of the CA bound to Arp2/ArpC1 (magenta) and Arp3 (violet). (A) C motifs. (B) A motifs. The flexible A motif has higher RMSF values than the C motif. Solid lines show average RMSD values and shaded regions indicate standard deviations of RMSD values across three replica runs. (C-E) Interactions between A motif residues D482 to D497 in the D/E loop with (C) Arp2, (D) ArpC1 and (E) Arp3. Color bars represent durations of the contacts on a timescale of ns. The longest interactions persisted for 2.5 µs in a 3.4 µs simulation. The interactions of A with Arp2/ArpC1 are more persistent than with Arp3. (F,G) The aromatic ring of conserved phenylalanine F493 of the A motif forms stacking interactions with (G) P190 of ArpC1 and its backbone amide hydrogen bonds with the carboxylate oxygen of E193 of ArpC1; and with (H) W252 of Arp3.

Section 5: Effect of CA binding to Arp2/3 complex on the dynamics of the Arps

Effect of CA binding on the dynamics of Arp2 and Arp3 is measured by root-mean-square-fluctuations (RMSF) (Fig. S5 A,B) during the 3.4 ns MD simulation. Numbers in Fig. S5A highlight regions of Arp3 with larger RMSF values with bound CA (pdbid: 6UHC) (red) than without CA (pdb id: 4JD2) (black): (1) loop following the hinge helix (R156-G165); (2) loop in SD3; and (3) loop in SD4. The difference in the RMSF in residues R156-G165 may be attributed to clashes of bumper-helix and D-loop during block rotation towards partially active state in the CA bound complex. No significant difference was observed in the RMSF of Arp2 residues with bound CA in Fig. S5B. The Arp2/3 complexes with and without bound CA were from different species, but their sequences are nearly identical.

CA binding makes small changes in the dihedral angles of Arp2 and Arp3. The dihedral angle formed by the four subdomains (SD2-SD1-SD3-SD4) of Arp2 is -8.6° and of Arp3 is -18.8° in the cryo-EM structure (Fig. S5 E,F). During the 3.4 µs simulation, Arp2 and Arp3 adopt a more twisted conformation with the dihedral angle of -16.1±4.0° for Arp2 and of -30.1±4.0° for Arp3. These values are similar to the dihedral angles measured in the MD simulation of inactive state with -19.8±3.4° for Arp2 and -28±3.3° for Arp3 (Fig. S3 E, F).

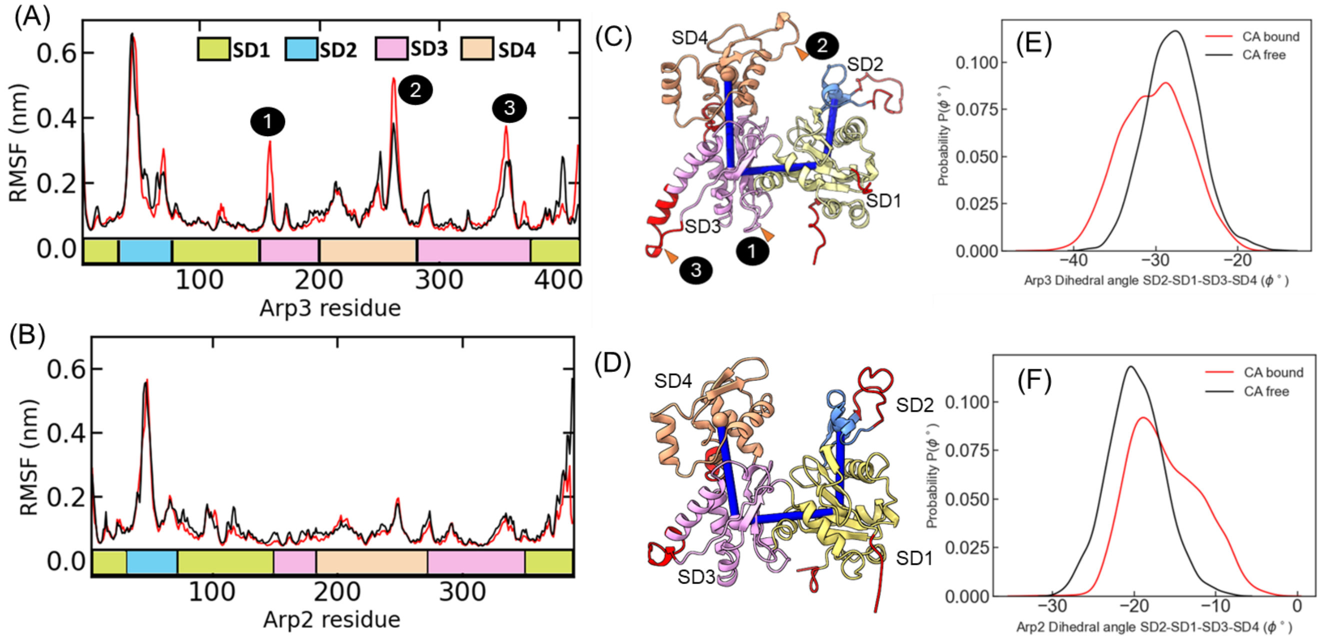

Figure S7. Comparison of the dynamics of Arp2 and Arp3 in inactive bovine Arp2/3 complex without CA (4JD2) during a 1 µs MD simulation and during the 3.4 *µs* of MD simulation of inactive human Arp2/3 complex bound to CA (pdb id: 6UHC). Bound CA changes the dynamics of local regions the Arps. (A,B) Time courses of residue Root Mean Square Fluctuations (RMSF) of the Arps without CA (black) and with bound CA (red). (A) Comparison of RMSFs of Arp 3 subunits. Three regions have different RMSF values with and without bound CA: (1) is Q157-E160; (2) is N260-K264; and (3) is S354-K361. (B) RMSFs of Arp2 subunits, showing no differences. (C,D) Ribbon diagrams show how Arp dihedral angles were calculated using lines between the centers of mass of SD2 (blue), SD1 (yellow), SD3 (pink) and SD4 (orange). Orange (Arp3) and red (Arp2) residues were not included for measuring the centers of mass(7). Regions in red indicate residues with high RMSF. Arrowheads in Arp3 (C) indicate residues with different RMSF values with and without bound CA. (E, F) Comparisons of SD2-SD1-SD3-SD4 subunit dihedral angles sampled during MD simulations by Arp2 and Arp3 subunits in the inactive state (pdb id: 4JD2; black) and CA bound state (pdb id: 6UHC, red). (E) Arp2 dihedral angles are -16.1±4.0° with CA and -19.8±3.4° without CA. (F) of Arp3 dihedral angles are -30.1±4.0° with CA and -28±3.3° without CA.

Effects of CA binding on collective fluctuations of the whole Arp2/3 complex

We used the K-Means Clustering Coarse Graining (KMC-CG) protocol (8) to evaluate the global dynamics of free bovine Arp2/3 complex (pdb id: 4JD2) with human Arp2/3 complex with bound CA (pdb id: 6UHC). The KMC-CG method preserves both spatial and dynamical features of the underlying all-atom trajectory. The mapping was generated by preserving the spatial distances and fluctuation of each pair of residues in the CA bound and unbound MD trajectories. Arp2/3 complex with and without bound CA are from different species, but their sequences are nearly identical.

The whole production trajectory of the CA-bound system was used to build the CG mapping. The mapped all-atom trajectories are obtained for both CA-bound and no-CA systems by locating the CG site at the center-of-mass of all C-alpha atoms which belong to that CG site. Then mapped all-atom trajectories were cut into six pieces of equal length. The first piece was excluded as relaxation. RMSF was calculated independently for each piece of trajectory, and the standard deviation error was calculated using the last five trajectories for each system.

Fluctuations of the mapped CG sites measure the amplitude of correlated motion in the CA bound and unbound conformations (Fig. S6). Note that these fluctuations differ from the per-residue RMSF in Fig. S4. The KMC-CG protocol groups together residues with correlated fluctuations, thus amplifying any small differences in per-residue RMSF shown in Fig. S5.

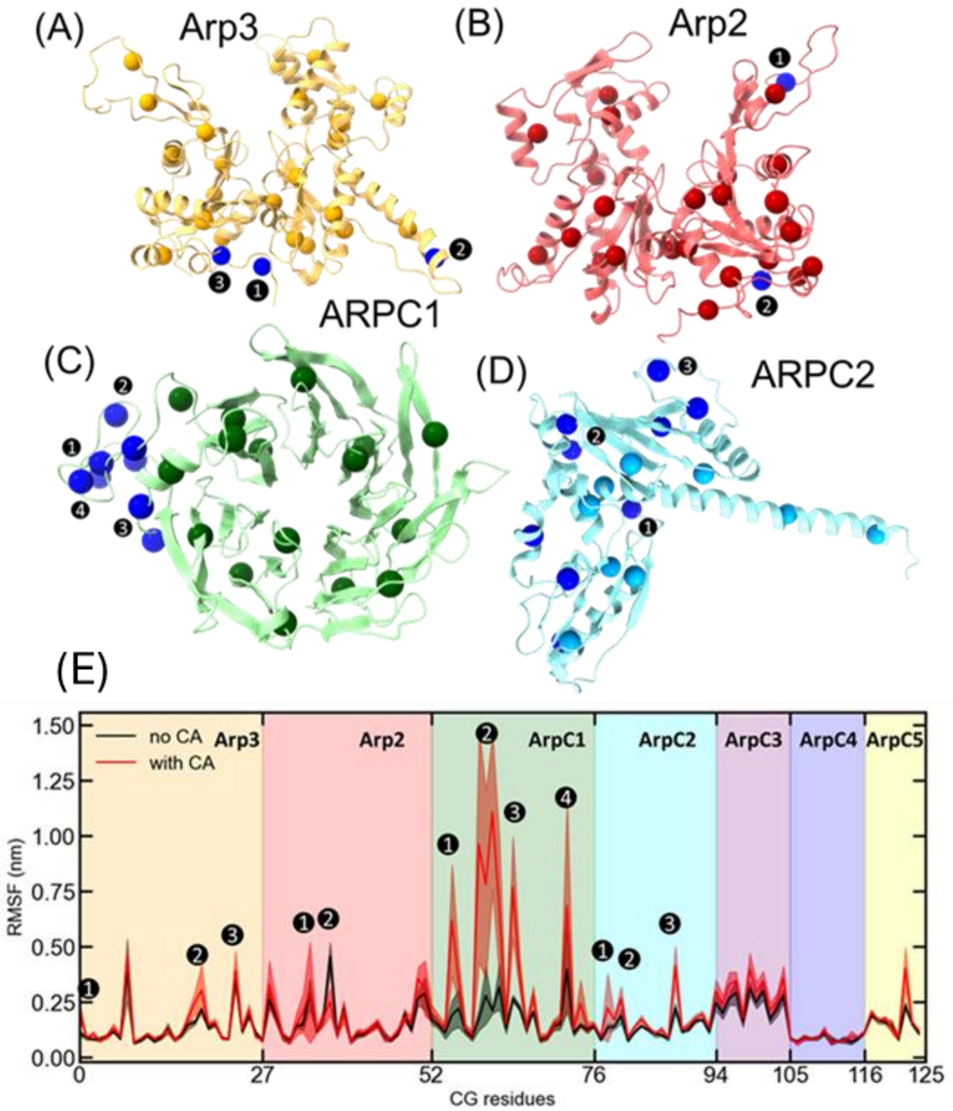

Figure S8. K-Means Clustering Coarse Graining (KMC-CG) simulations of Arp2/3 complex identify effects of CA binding on correlated fluctuations. White numbers on black in A-E label CG sites in Arp3, Arp2, ARPC1 and ARPC2 subunits that differ significantly in the residue mean squared fluctuations (RMSF) between the CA bound and free Arp2/3 complex. (A-D) Ribbon diagrams showing as spheres the coarse grain (CG) sites of subunits Arp3, Arp2, ARPC1 and ARPC2. The sites were selected using an approximate resolution of 15 amino acids per site. The CG sites are numbered continuously: Arp3: 0-26 (orange), Arp2: 27-51 (red), ARPC1: 52-75 (green), ARPC2: 76-93 (cyan), ARPC3: 94-104 (purple), ARPC4: 105-115 (blue) and ARPC5: 116-125 (yellow). (E) Graph of RMSF for the coarse grain sites across all seven subunits for (black) free bovine Arp2/3 complex (pdb id: 4JD2) and human Arp2/3 complex with bound CA (pdb id: 6UHC). Shaded areas correspond to the standard deviation in the fluctuations calculated by splitting the trajectory into six blocks of equal length. The first piece is excluded as relaxation.

CA binding produces significant differences in the RMSF for the C-terminal tail (Fig. S6 peaks 1 and 2) and the bumper helix regions (Fig. S6 peak 3) of Arp3. The variance in the D-loop fluctuations of Arp2 are higher with bound CA (Fig. S6 peak 1 of Arp2). The bumper helix interacts with the D-loop of Arp2 in the transition state model of Arp2/3 complex. Larger fluctuation amplitudes of the bumper helix with bound CA may indicate a role for CA in shifting the equilibrium population towards the transition state. Bound CA also increased fluctuations of the C-terminal tail of Arp3 as expected from interactions with N-terminus of the C-helix Fig. 4, which also has greater fluctuations.

The largest differences with and without bound CA are in the insert helix of ArpC1, which mapped into several CG sites (Fig. S6 peaks 1-4 of ArpC1;). The fluctuations did not differ significantly for ArpC3 or ArpC4 with free or CA bound Arp2/3 complex. The large RMSF difference of ArpC5 with bound CA is in the flexible N-terminal region.

Taken together, CA binding to Arp2/ArpC1 and Arp3 affects the dynamics throughout Arp2/3 complex, which may contribute to shifting the conformation of the equilibrium population away from the inactive state.

Section 6: Effect of actin monomer on the transition state Arp2/3 complex

We used hetero Elastic Network Modelling (hENM) to measure the strength of interactions between the subunits in the transition state of Arp2/3 complex in terms of the effective spring constants. Actin binding has a non-linear effect on the inter-subunit interactions (Fig. S7E). With a bound actin monomer inter-subunit interactions are weaker between Arp3-ARPC2, Arp3-ARPC3 and Arp2-ARPC1 and stronger between Arp2-Arp3, Arp3-ARPC4, ARPC1-ARPC4 and ARPC1-ARPC5.

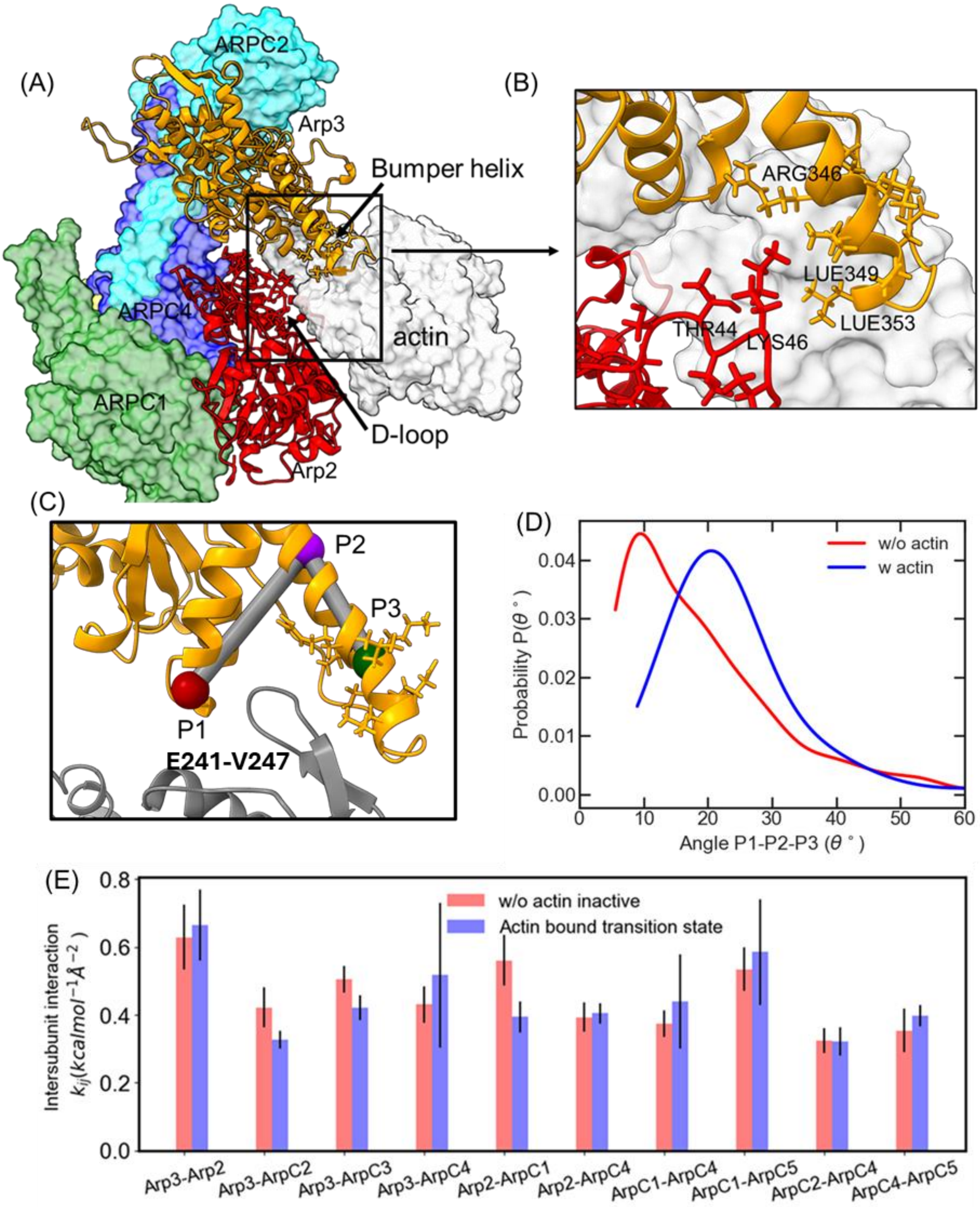

Figure S9: Characterization of the transition state structure with a bound actin monomer. (A) Space-filling and ribbon diagram of Arp2/3 complex in the transition state (pdb id: 7T5Q) with a bound grey space-filling actin monomer. The D-loop of Arp2 (residues 37-50) and bumper helix of Arp3 (residues 346-353) rendered as stick figures. (B) Detail of the actin bound between Arp3 and D-loop of Arp2. The bound actin reduces clashes between T44 and K46 in the D-loop and the bumper helix residues R346, L349, and L353. (C) The loop (E241-V247) in SD4 of actin monomer (gray) wedges between the bumper helix and the adjacent of Arp3 (orange), displacing the bumper helix as measured by the angle formed by points P1,P2 and P3. P1 is the center of mass of residues M306-I310 in the adjacent helix, P2 is the center of mass of residues Q336 to T342 on the long helix bumper helix, and P3 is the center of mass of residues R346 to L353 on bumper helix. (D) Comparison of the distribution of angles formed by P1-P2-P3 in the actin bound complex (average of 27.6° and the inactive state (average 20.5°) upon removing actin. The slight twisting that displaces the bumper helix leaves space for the movement of Arp2 block without the clashes between D-loop and bumper helix. (E) Inter-subunit interactions obtained from hENM modelling of the transition state complex with bound actin monomer (blue) and in the trajectory after the complex reverts into the inactive, splayed state upon removing actin(red). Each subunit is modelled as a coarse grain site at the center of mass of the subunit connected by harmonic bonds (k_{ij}). The effective spring constant of the harmonic bonds measures the inter-subunit interaction strength. Error bars indicate standard deviations in (k_{ij}) calculated by splitting the trajectory into blocks of length 200 ns.

Section 7: Analysis of surface area (Å²) buried between subunits of Arp2/3 complex and the mother filament subunits M1-M6.

Structures of ARPC2 and ARPC4 from models partially active and inactive Arp2/3 complex were docked onto the mother filament by aligning the Arp3 subdomains 3 and 4 with the branch junction structure (Fig. S8). These outer subdomains of Arp3 were used for docking, since this superposition was used earlier to visualize rotation of the lower block during the rotation to the short-pitch state (Fig. 5D,E). Furthermore, docking by the superposition of ARPC2 and ARPC4 results in a number of clashes between the other subunits of the Apr2/3 complex and the mother filament subunits. The buried surface area between Arp2/3 complex and the mother filament is 3500 $Å^2$ in the branch junction, 1700 $Å^2$ in the docked inactive complex and 1900 $Å^2$ in the docked partially active complex. The 12.1° rotation of the two structural blocks of Arp2/3 complex causes 200 $Å^2$ increase in buried surface and may contribute to the higher affinity of Arp2/3 complex with bound CA for the side of the actin filament.

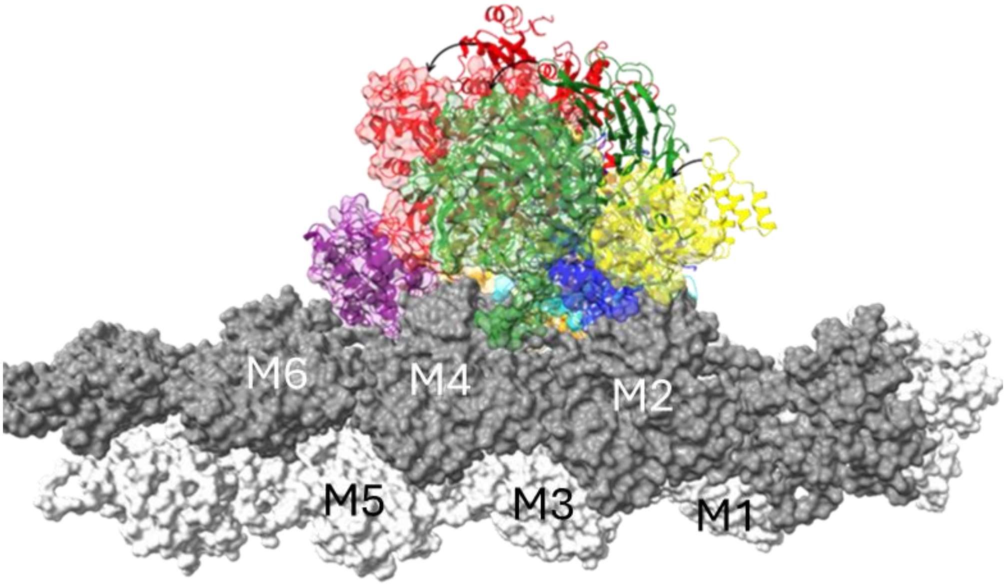

Figure S10: Docking partially active Arp2/3 complex on the mother filament. The subdomains 3 and 4 of Arp3 subunit were used to superimpose and align partially active Arp2/3 complex in the branch junction. Superposition results in the docking of ArpC2 (cyan) and ArpC4 (blue) of the partially active complex on to the mother filament. Active Arp2/3 complex in the branch junction (pdb id 7TPT) is shown in a transparent space filling model. The partially active state resulting from the 3.4 µs simulation of CA bound Arp2/3 complex (pdbid: 6UHC) is shown as ribbons. An arrow indicates the conformational change from the partially active state to the active state by rotation of the block containing Arp2 (red), ARPC1 (green) and ARPC5 (yellow).

References

1. S. C. Panchal, D. A. Kaiser, E. Torres, T. D. Pollard, M. K. Rosen, A conserved amphipathic helix in WASP/Scar proteins is essential for activation of Arp2/3 complex. *Nat Struct Biol* **10**, 591-598 (2003).
2. A. Zimmet *et al.*, Cryo-EM structure of NPF-bound human Arp2/3 complex and activation mechanism. *Sci Adv* **6** (2020).
3. S. C. Ti, C. T. Jurgenson, B. J. Nolen, T. D. Pollard, Structural and biochemical characterization of two binding sites for nucleation-promoting factor WASp-VCA on Arp2/3 complex. *Proc Natl Acad Sci U S A* **108**, E463-471 (2011).
4. J. B. Marchand, D. A. Kaiser, T. D. Pollard, H. N. Higgs, Interaction of WASP/Scar proteins with actin and vertebrate Arp2/3 complex. *Nat Cell Biol* **3**, 76-82 (2001).
5. H. I. Balcer, K. Daugherty-Clarke, B. L. Goode, The p40/ARPC1 subunit of Arp2/3 complex performs multiple essential roles in WASp-regulated actin nucleation. *J Biol Chem* **285**, 8481-8491 (2010).
6. Q. Luan, A. Zelter, M. J. MacCoss, T. N. Davis, B. J. Nolen, Identification of Wiskott-Aldrich syndrome protein (WASP) binding sites on the branched actin filament nucleator Arp2/3 complex. *Proc Natl Acad Sci U S A* **115**, E1409-e1418 (2018).

7. M. Shaaban, S. Chowdhury, B. J. Nolen, Cryo-EM reveals the transition of Arp2/3 complex from inactive to nucleation-competent state. *Nature Structural & Molecular Biology* **27**, 1009-1016 (2020).
8. J. Wu, W. Xue, G. A. Voth, K-Means Clustering Coarse-Graining (KMC-CG): A Next Generation Methodology for Determining Optimal Coarse-Grained Mappings of Large Biomolecules. *J Chem Theory Comput* **19**, 8987-8997 (2023).